Published by IOP Publishing for Sissa Medialab

Received: *December 2, 2019*
Revised: *January 13, 2020*
Accepted: *January 18, 2020*
Published: *February 11, 2020*

MOGA optimization for the ILSF low-beta lattice storage ring

S. Dastan,[a,b,1] **E. Ahmadi,**[b] **A. Mash'al,**[b] **J. Rahighi**[b] **and R. Saffari**[c]

[a] *University of Guilan, Campus2, 4199613776 Rasht, Iran*
[b] *Iranian Light Source Facility, Institute for Research in Fundamental Sciences, 19395-5746 Tehran, Iran*
[c] *Department of Physics, University of Guilan, 41335-1914, Rasht, Iran*

E-mail: saradastan@phd.guilan.ac.ir

Abstract: In this paper, The Multi-Objective Genetic Algorithm (MOGA) is employed to optimize a low-beta lattice for the storage ring of the Iranian Light Source Facility (ILSF) [1]. This technique is based on tracking particles to select the working tune points and the appropriate sextupoles strengths, which in turn improve Dynamic Aperture (DA) and Momentum Acceptance (MA). In addition, we utilize Frequency Map (FMA) and tune scan to optimize MOGA results. Furthermore, the effect of multiple errors due to magnetic elements and Insertion Device (ID) is studied in the ILSF storage ring and the details of beam parameter variation because of the errors and an in-vacuum undulator are discussed. The results show that by applying the MOGA, DA and Toscheck lifetime improve.

Keywords: Accelerator Applications; Beam dynamics; Beam Optics

[1]Corresponding author.

https://doi.org/10.1088/1748-0221/15/02/P02009

2020 JINST 15 P02009

Contents

1 Introduction **1**

2 Theory of nonlinear beam dynamics **3**

3 MOGA algorithm and sorting method **4**

4 The low-beta lattice **5**

5 Nonlinear optimization results for bare lattice **7**

6 Effect of errors and insertion device on the optimized lattice **11**

7 Conclusion **19**

2020 JINST 15 P02009

1 Introduction

Iranian Light Source Facility is the 4^{th} generation synchrotron light source in the design stage. ILSF storage ring lattice is a five bend achromat lattice with a circumference of 528 m and natural emittance of 270 pm-rad. There are two proposed lattices for the ILSF storage ring, the existing [2] and the low-beta lattice. In this paper, the low-beta lattice will be described and optimized for the ILSF storage ring, which is actually high- and low-beta lattice. The high beta straight is suitable for injection, and the low beta straight for ID to improve brightness. To meet the user's demands [3] in the future, i.e. providing high brilliance photon source and a beam with a small emittance, is necessary. In order to increase brightness in the low-beta lattice, the betatron functions in some straight sections should be decreased. Also, the efficient way to minimize emittance is to adjust quadrupole strength to obtain the minimum emittance, which is achieved by OPA [4] in the low-beta lattice. As a result, the emittance remains constant in comparison with the existing lattice, the optic function, and the main parameters of these two lattices are shown in figure 1 and table 1. Figure 1b shows that the low-beta lattice includes 9 families of quadrupoles and 10 families of sextupoles with a symmetric mirror structure that the ILSF storage ring constitutes by 10 low-beta supercells. The significant change in the low-beta lattice is the horizontal beta function which decreases in the long straight section of the low-beta lattice. In addition, because of different types of straight sections (short and long) in the low-beta lattice, the periodicity reduces to 2. The first modification improves the brightness of the emitted photon from Insertion Devices (IDs), the comparison of the brightness from ID in the existing and the low-beta lattice is illustrated in figure 2. However, in virtue of strong sextupole magnets and decreased supersymmetry from 20 to 10 in comparison with the existing lattice, the low-beta lattice has a weak performance with small DA, MA, and poor injection efficiency.

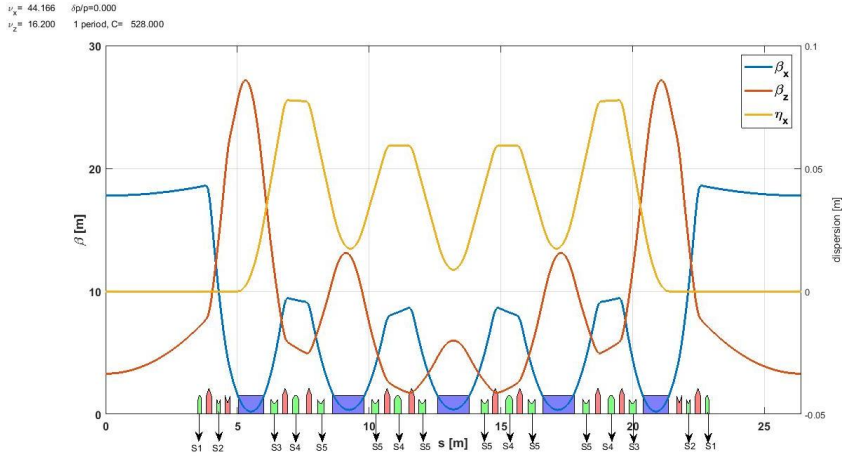

(a) Twis parameters in existing lattice

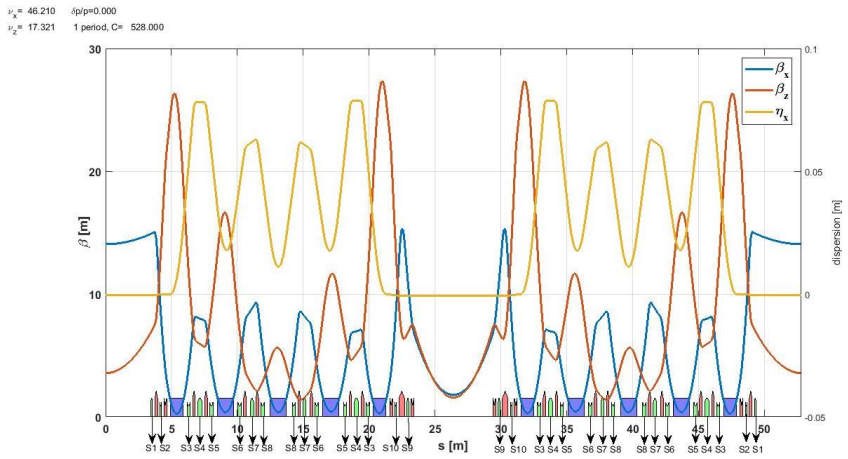

(b) Twis parameters in low-beta lattice

Figure 1. Twiss parameters in the existing and the low-beta lattice by assigning the location of sextupoles.

The Genetic Algorithm (GA) has been applied to improve the parameters of the low-beta lattice. This algorithm has been used in a wide range of engineering and industrial applications. GA also has been employed in the accelerator field since 1992 [6], to optimize the injector design of Cornel energy recovery linac-based light source [7] or to improve the laser parameters for a photoinjector gun [8–10]. It has been applied to balance design and operating costs of a superconducting rf, too [11, 12]. It also has a role in optic optimization in advance photon source [13] and free-electron laser applications [6].

In sections 2 and 3 of this paper, we will address briefly non-linear theory and genetic algorithm. In section 4, we introduce the low-beta lattice in more details, while in section 5, the optimization results are discussed. Also, in section 6, we will study different types of errors and the effect of insertion device on the different parameter of the machine. Finally, we summarize the results in section 7.

2020 JINST 15 P02009

Table 1. Main parameters of both lattices.

Parameters	Unit	Existing Lattice (EL)	Low-beta Lattice (LBL)
Beam Energy	GeV	3	3
Natural horizontal beam emittance	pm-rad	270	276
Lattice structure	-	5BA	5BA
Number/length of straight sections	-/m	20*7.0	10*6.87/10*6
Natural energy spread	-	6.80×10^{-4}	6.80×10^{-4}
Momentum compaction factor	-	1.82×10^{-4}	1.904×10^{-4}
2nd order Momentum compaction factor	-	3.82×10^{-4}	2.99×10^{-4}
Tune(Q_x/Q_y)	-	44.16/16.22	46.27/17.32
Natural chromaticity (H/V)	-	−107.79/−61.45	−99.301/−64.623
Horizontal damping partition J_x	-	1.38	1.40
RF frequency	MHz	100	100
Coupling	%	1.0	1.0
Beam size at the straight section (H/V)	μm	68.92/2.96	61.30/3.30
Beam divergence at the straight section (H/V)	μrad	3.87/0.90	4.52/0.83
Maximum beam current	mA	400	400

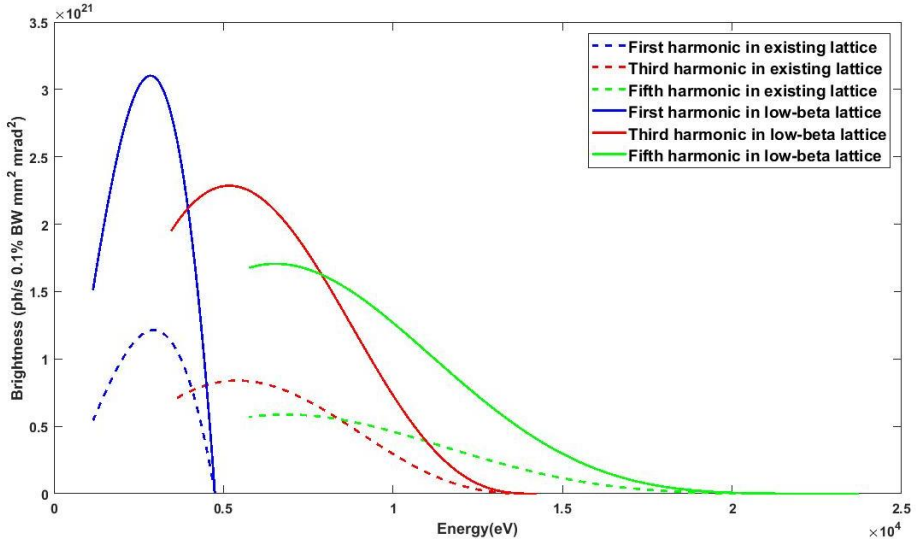

Figure 2. Comparison of the brightness from ID in the existing and the low-beta lattice. The calculation is done by SPECTRA [5].

2 Theory of nonlinear beam dynamics

In the course of the preliminary optimization, we have used 10 different families of sextupoles in the low-beta lattice. The following Hamiltonian can explain the nonlinear effect of the sextupoles on the motion of particles [14]

$$H(s) = \frac{p_x^2 + p_y^2}{2(1+\delta)} - b_1 x\delta + \frac{b_1^2}{2}x^2 + \frac{b_2}{2}(x^2 + y^2) + \frac{b_3}{3}(x^3 - 3xy^2) + O(4) \tag{2.1}$$

2020 JINST 15 P02009

where $p_{x/y}$ is the momentum of a particle, b_2 and b_3 are quadrupole and sextupole magnetic field component respectively, and δ is momentum deviation. Also, $\frac{b_3}{3}(x^3-3xy^2)$ demonstrates sextupoles' Hamiltonian, and $\frac{b_2}{2}(x^2+y^2)$ represents Hamiltonian of quadrupoles. Eq. (2.1), is expanded up to third order, for higher-order multipoles Hamiltonian, the expansion should be continued.

Applying the perturbation theory, the first order Hamiltonian in the presence of quadrupoles and sextupoles can explain by Resonance Driving Terms (RDTs) as below

$$h_{jklmp} \propto \sum_{n}^{N_{\text{sext}}} (b_3L)_n \beta_{xn}^{\frac{j+k}{2}} \beta_{yn}^{\frac{l+m}{2}} \eta_n^p e^{i[((j-k)\phi_{xn}+(l-m)\phi_{yn})]} - \sum_{n}^{N_{\text{quad}}} (b_2L)_n \beta_{xn}^{\frac{j+k}{2}} \beta_{yn}^{\frac{l+m}{2}} e^{i[(j-k)\phi_{xn}+(l-m)\phi_{yn}]} \tag{2.2}$$

that j, k, and l are the integer numbers. Also, $\beta_{x/y}$ and $\phi_{x/y}$ are beta function and phase advance, respectively. One can see that h_{11001} and h_{00111} are independent of phase advance and they are called first-order or linear chromaticity

$$h_{11001/00111} = \xi^1_{x/y} = \mp\frac{1}{4}\sum_{k=1}^{N}[(b_2L)_k - 2(b_3L)_k\eta_{x,k})]\beta_{(x/y),k} \tag{2.3}$$

which k-indices show the beta function and dispersion in the position of k-magnet. We have used two families of sextupoles ($S3$, $S4$), for correcting linear chromaticity. The second order of chromaticity which is formulated as below

$$\xi^2_{x/y} = -\frac{1}{2}\xi^1_{x/y} + \frac{1}{8\pi}\sum_{k=1}^{N}\left[2(b_3L)_k\frac{\partial\eta_{x,k}}{\partial\delta}\beta_{(x,y),k} - \left[(b_2L)_k - 2(b_3L)_k\eta_{x,k}\right]\frac{\partial\beta_{(x,y),k}}{\partial\delta}\right] \tag{2.4}$$

leads to an incoherent betatron tune spread, and it can produce Landau damping of transverse instabilities [15]. One thing which is clear from the second order of chromaticity equation is that the considerable variation of dispersion and betatron function will increase the value of second-order of chromaticity. In fact, the higher order of chromaticity causes the particles not to act appropriately in the storage ring, for compensating the effect of second-order of chromaticity and improving other parameters in the lattice the other families of sextupoles (S1, S2, S5, S6, S7, S8, S9, S10) are applied. As one can see from figure 1b, (S1, S2, S9, S10) are placed in the dispersion free region and (S3, S4, S5, S6, S7, S8) are located in dispersion region, these two groups of sextupole families are called geometric and chromatic respectively.

3 MOGA algorithm and sorting method

The GA algorithm is employed in two different ways. The single objective optimization problem which presents a single solution and multi-objective optimization problems which produce a set of solutions [16]. In this paper, we deal with some parameters which need to be optimized, and it means that the multi-objective optimization problem in GA is applied. One can formulate MOGA

2020 JINST 15 P02009

as below

$$\begin{aligned} &\text{Min or Max} && F_n(x), && n = 1, 2, \ldots, N \\ &\text{subject to} && H_k(x) \geq \text{ or } \leq 0, && k = 1, 2, \ldots, K \\ & && G_j(x) = 0, && j = 1, 2, \ldots, J \\ & && x_i^L \leq x_i \leq x_i^U && i = 1, 2, \ldots, n. \end{aligned} \tag{3.1}$$

where F_n are the objectives, H_k and G_j are the inequality and equality constraints. Also, x_i^U and x_i^L are upper and lower bounds on variables. In this algorithm, a group of individuals which are represented by $x = (x_1, x_2, \ldots, x_n)^T$, creates population and successive populations are generation [17]. GA generates a set of populations in an objective surface which is called Pareto front without any domain or ranking knowledge, but the user needs more criteria for choosing the solutions or sorting them from best to worst, this is done by sorting algorithm.

Some of the most important sorting algorithms which improved MOGA are discussed in refs. [18–20]. **NSGA-II** which has been proposed by Deb et all in 2000, uses in this work for sorting the solutions. This algorithm is propounded as a new version of NSGA [21].

Rank and Crowding Distance (CD) are the first two main parameters in NSGA-II which should be defined for each individual in the population. Rank is the level of non-domination and it can be explained as: consider $x^{(i)}$ and $x^{(j)}$ as two solutions for eq. (3.1), one can say that $x^{(i)}$ dominates $x^{(j)}$ when $x^{(i)}$ acts better than or as same as $x^{(j)}$ for all the objectives and exactly in one objective $x^{(i)}$ shows better result than $x^{(j)}$. If two solutions do not dominate each other, they are placed in the same rank.

The other parameter for sorting in NSGA-II is CD which is explained as the measure of solution's density [22] and it defines as follows

$$\begin{aligned} d_1^i &= \frac{F_1^{i+1} - F_1^{i-1}}{F_1^{\max} - F_1^{\text{Min}}} \\ d_2^i &= \frac{F_2^{i+1} - F_2^{i-1}}{F_2^{\max} - F_2^{\text{Min}}} \end{aligned} \tag{3.2}$$

The crowding distance is $d^i = d_1^i + d_2^i + \ldots$. The parameters of eq. (3.2), are shown in figure 3. Defining rank and CD for each solution, the parents choose based on the Binary tournament selection. It means that between two solutions x_1 and x_2, the solution with lower rank is selected. However, if the rank of the solutions is the same, the solution with higher CD is preferred, as spatially distributing samples points is a crucial consideration in most sampling algorithm, CD measures the relative isolation of $\overrightarrow{x}$ from a given i points, the greater the CD, the greater is its isolation [20].

4 The low-beta lattice

The effective beam emittance for a soft x-ray light source is related to twiss parameters and natural emittance as follow [23]

$$\varepsilon_z^{\text{eff}} = \sqrt{\varepsilon_z^2 + \varepsilon_z \left(\beta_z + \frac{\frac{L^2}{4\pi^2} + \sigma_E^2 \eta_z^2 \frac{2L}{\lambda}}{\beta_z} \right) \frac{\lambda}{2L} + \frac{\lambda^2}{16\pi^2} + \sigma_E^2 \eta_z^2 \frac{\lambda}{2L}} \tag{4.1}$$

2020 JINST 15 P02009

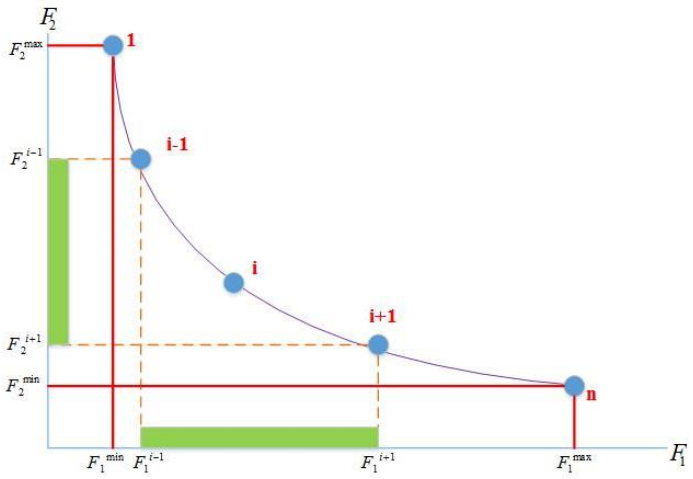

Figure 3. Definition of Crowding distance in NSGA-II.

where $z = x, y$, ϵ_z is natural emittance, σ_E is energy spread, β_z is twiss function, η_z is dispersion, L is the undulator length and λ is the radiation wavelength. From figure 1b, one can see that the dispersion function is zero in straight sections, so the effective emittance in straight sections becomes

$$\varepsilon_z^{\text{eff}} = \sqrt{\varepsilon_z^2 + \varepsilon_z \left(\beta_z + \frac{\frac{L^2}{4\pi^2}}{\beta_z}\right) \frac{\lambda}{2L} + \frac{\lambda^2}{16\pi^2}} \tag{4.2}$$

In order to increase brightness, it is needed to reduce the effective beam emittance, since the brightness is inversely proportional to the effective beam emittance. From eq. (4.2), for minimizing the effective beam emittance, natural emittance should decrease. Also, there is an optimum value for β_z which minimizes $\varepsilon_z^{\text{eff}}$ and calculates as follows

$$\frac{\partial \varepsilon_z^{\text{eff}}}{\partial \beta_z} = 0 \implies \beta_{z_{\text{opt}}} = \frac{L}{2\pi} \tag{4.3}$$

minimizing the natural emittance and optimizing the beta function in order to improve the brightness from the IDs, are the main alterations of the low-beta lattice.

In working with MOGA, the working tune points influence on the speed of the answer's convergence, as well as finding an optimal solution. So, we analyze tune scan in order to select the best working tune points based on DA area and Touscheck lifetime. Scanning the working tune points is done by varying the strength of one focusing and one defocusing quadrupole, which does not affect the zero dispersion in the straight sections. For each tune, DA and MA track and Touscheck lifetime calculates based on the result of MA tracking. We scan ν_x and ν_y from $(46.01, 17.01)$ to $(46.60, 17.60)$. One can see from figure 4, the working tune points [46.21–46.24] for ν_x and [17.21–17.24] for ν_y have DA area near to 70 μm^2 and Touscheck lifetime more than 1 hour. Based on the scanning [46.21–46.24] and [17.21–17.24] for ν_x and ν_y respectively, are the best choice for working tune points. Also, to minimize the effect of 3^{rd} and 4^{th} order betatron resonances, the target working point is chosen slightly far from 0.25. So, the tunes and their ranges, are the first constraints in MOGA optimization.

2020 JINST 15 P02009

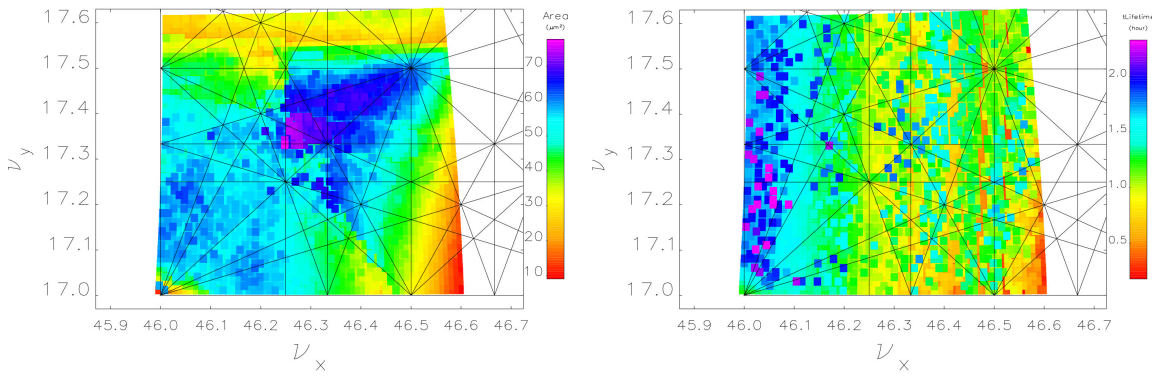

(a) Tune scan based on the DA area

(b) Tune scan based on the Touscheck lifetime

Figure 4. Tune scan based on Touscheck lifetime and DA area.

The second constraint which should consider in optimization is betatron function that many parameters are dependent on it like RDTs, stop bandwidths, linear orbit error amplification factors, etc. [24, 25]. Also, it affects injection efficiency and brightness of the lattice. Therefore, we put a restriction on the maximum beta functions in vertical and horizontal planes by two other quadrupoles magnet as below

$$\begin{aligned} \beta_{x_{\max}} &< 25(m) \\ \beta_{y_{\max}} &< 30(m) \end{aligned} \tag{4.4}$$

The other constraints in order to avoid large tune-spread due to energy errors and to suppress the transverse head-tail instabilities is the first-order natural chromaticity which should be corrected and brought close to zero by sextupole magnets.

To fulfill the mentioned constraints, four quadrupoles, and two sextupoles families have used, the quadrupoles are selected based on their effect on dispersion and emittance. In designing stage of the low-beta lattice and tunning the parameters by OPA, we find out that changing the strength of some quadrupoles will change the twiss parameters, especially the natural emittance and dispersion in straight sections dramatically. Based on this perception, we choose one focusing and one defocusing quadrupole in dispersion free region to correct the working tune points, as well as two focusing quadrupoles in high dispersion region to restrict the maximum beta function in vertical and horizontal planes. In accordance with section 2, (S3, S4) are used to correct linear chromaticity, and the other sextupoles are applied for compensating the second-order of chromaticity and optimizing DA and MA. Also, since these sextupoles compensate for the linear chromaticity, other sextupoles used as a variable parameter to optimize the area of DA, MA, and compensate for the effect of second-order chromaticity.

5 Nonlinear optimization results for bare lattice

DA defines as the area in the transverse plane in which the particles are stable after a given number of turns [26]. Besides, MA is the maximum momentum deviation that a particle can experience without becoming unstable and being lost [27]. The Touschek lifetime must compute by taking

2020 JINST 15 P02009

Table 2. Type and rate of magnet errors during the MOGA optimization.

Magnet	Type of Error	Rate of Error	Unit
Quadrupoles	FSE	$4e-4$	-
	$TILT$	$1e-4$	RAD
Sextupoles	FSE	$4e-4$	-
	$TILT$	$1e-4$	RAD

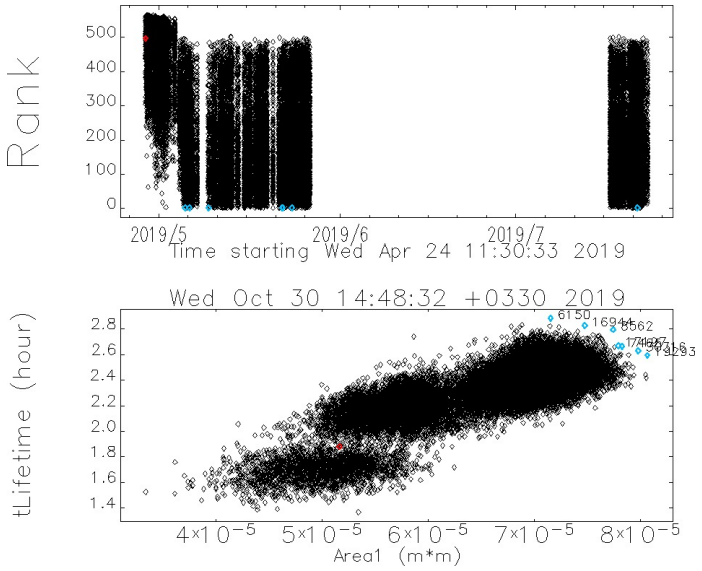

Figure 5. Rank of the solutions, DA area Touschek lifetime during MOGA optimization.

Table 3. The five best solutions in MOGA optimization.

runID	ν_x	ν_y	$\beta_{x_{\max}}$ (m)	$\beta_{y_{\max}}$ (m)	DA_{area} (m^2)	tLifetime (h)
6150	46.2106	17.3251	15.1147	25.9793	$7.16e-05$	2.8814
8562	46.2099	17.3233	15.0634	25.9604	$7.75e-05$	2.7940
19293	46.2100	17.3216	15.0595	25.9568	$8.07e-05$	2.5917
16944	46.2099	17.3225	15.0610	25.9582	$7.48e-05$	2.8244
17197	46.2099	17.3217	15.0589	25.9569	$7.79e-05$	2.6685

into account the positive and negative momentum acceptances. The area of dynamic aperture and Touschek lifetime are two objectives in MOGA optimization, which have been assessed during the optimization, during the MOGA optimization some tiny errors e.g., FSE[1] and TILT[2] errors for quadrupoles and sextupoles, as well as the effect of RF and SR are considered to find the robust solution. The errors which considered in the MOGA optimization are presented in table 2.

The results of the MOGA optimization are pictured in figure 5 and the five best solutions of the optimization present in table 3.

[1]Fractional strength error.
[2]Rotational about longitudinal axis.

2020 JINST 15 P02009

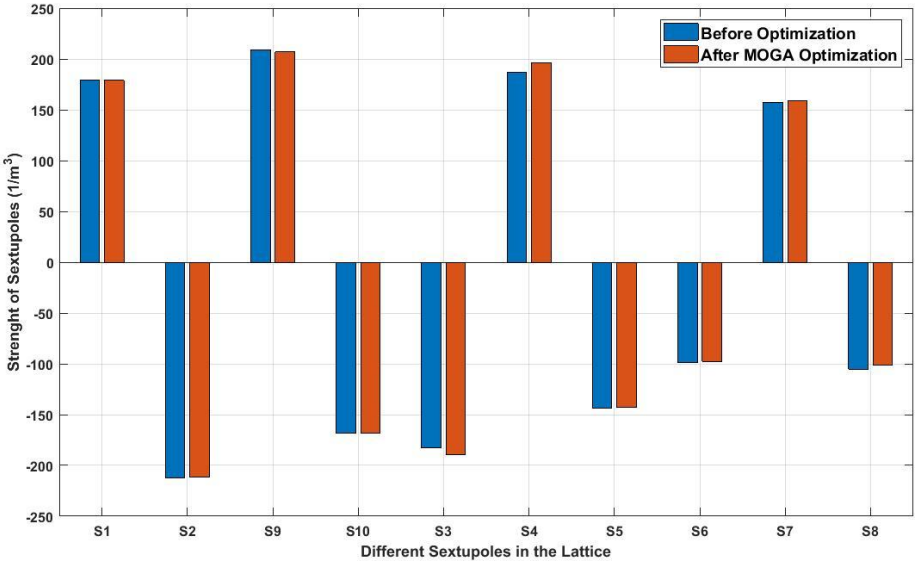

Figure 6. Variation of sextupoles strengths in MOGA optimization.

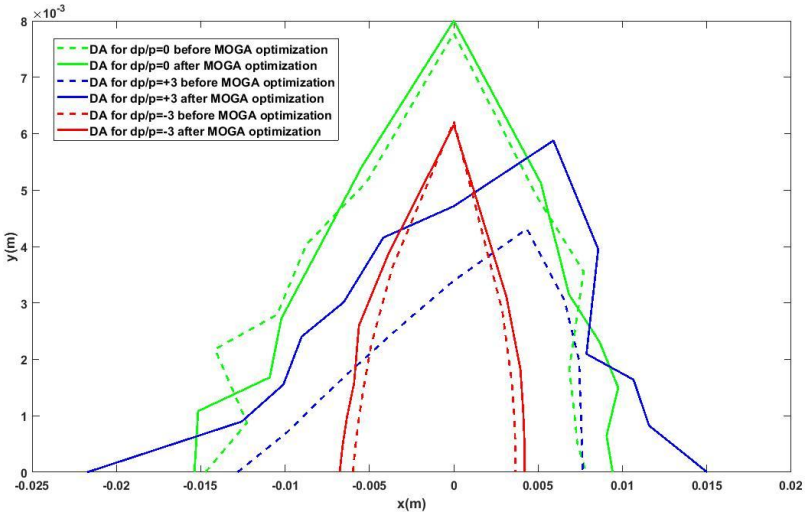

Figure 7. DA before (dashed-line) and after (solid-line) MOGA optimization.

The optimization and searching for the best solution carried out for about 25000 jobs, in each job submission 200 jobs submitted, so the optimization process took more than four weeks.

Among the five best solutions, we select the solution with the greatest area of DA as a final result of optimization. The variation sextupoles strengths after optimization in runID 19293, which considers as a final result, is shown in figure 6. The tracking is done with ELEGANT [28]; also we use the SDDS TOOLKIT [29] program and MATLAB, to plot the results of ELEGANT tracking.

The bare lattice DA of final solution for on-momentum ($\frac{dp}{p}=0$) and off-momentum ($\frac{dp}{p}=\pm 3\%$) particles is presented in figure 7, also the local MA before and after MOGA optimization is plotted in figure 8. The analyzes show improvement in the area of DA, as well as local momentum acceptance (LMA) in comparison with the initial low-beta lattice. However, based on the size of the vacuum

2020 JINST 15 P02009

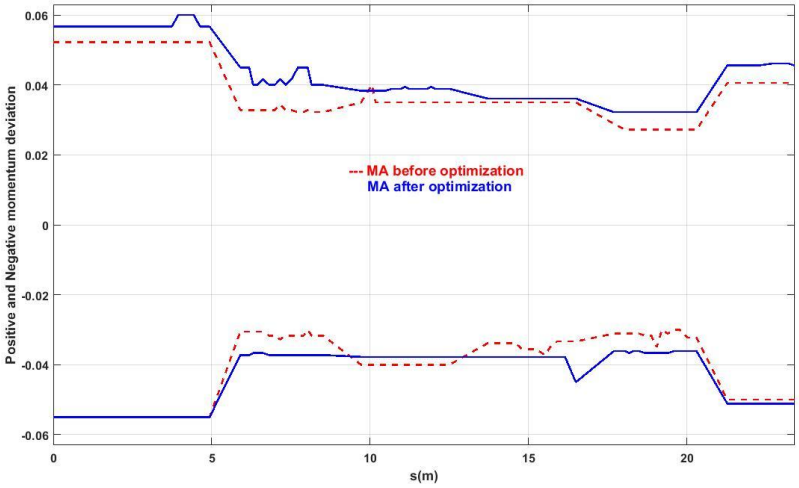

Figure 8. Momentum acceptance in one period before (dashed-line) and after (solid-line) MOGA optimization by considering the effect of RF, SR and some tiny errors 2. The Touschek lifetime for the optimized lattice is 2(h).

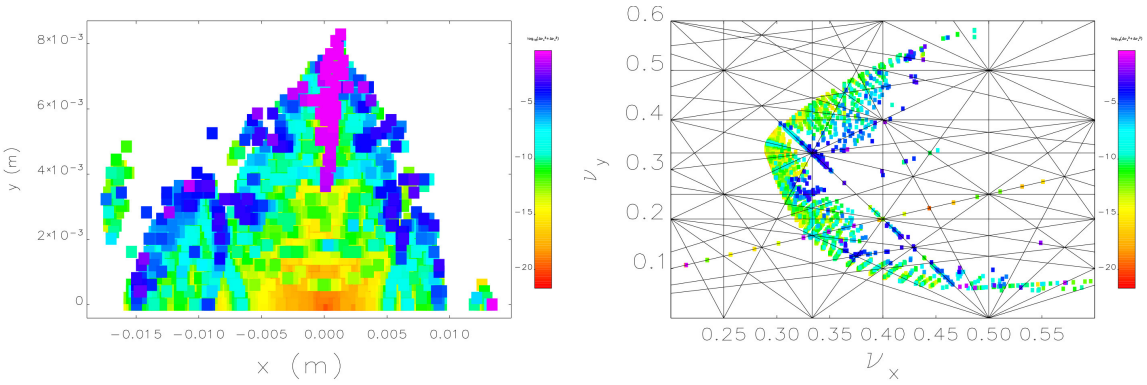

(a) **(b)**

Figure 9. DA and Tune of the optimized lattice based on the diffusion.

chamber, which is considered 10*mm* in simulation, one of the desired goals in the optimization is at least 10*mm* length of DA in the x-direction, which did not achieve after 25000 jobs of optimization. So, we started to check some parameters of the final result to find a way to improve the result of optimization. We commence with tune-scan, which we had done it before starting the optimization too. In this stage, we scan tunes for a wide range of numbers to see if there are any better working tune points. We track tune for 46–49 in x plane and 16–19 in y plane. The results show that the tune for y plane should change a bit from (17.31–17.34) to (17.32–17.39) that a slight variation in quadrupoles strengths does it.

The frequency map applies in this stage for finding the dangerous resonance and checking the tune shift [14]; the results are pictured in figure 9. In figure 9, one can see that for each point in the (x, y) aperture there corresponds a point in the (Q_x, Q_y) plane, the color code gives a measure of the stability of the particle (purple = unstable; red = stable). The indicator for the stability is given

2020 JINST 15 P02009

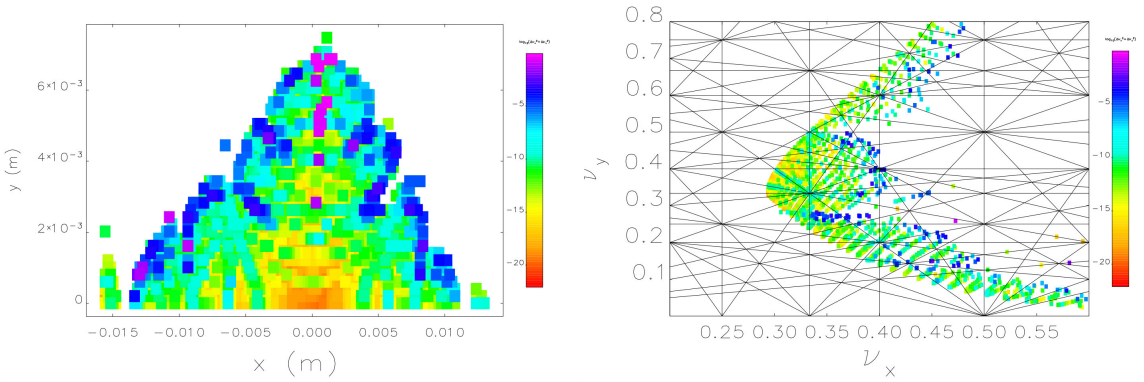

(a) **(b)**

Figure 10. FMA after optimization the lattice with OPA.

by the variation of the betatron tune during the evolution: i.e., tracking N turns we compute the tune from the first $\frac{N}{2}$ and the second $\frac{N}{2}$ that call it diffusion

$$D = \log_{10} \sqrt{(Q_x^2 - Q_x^1)^2 + (Q_y^2 - Q_y^1)^2} \tag{5.1}$$

It is clear from figure 9 that some particles have chaotic movement for a range of values in x and y directions. We figure out by comparing the plots in figure 9, that the $3rd$ and $4th$ order resonances cause the chaos motion. OPA code is applies for changing the weight factors of two first-order geometric terms e.g., $Q_x - 2Q_y$, $Q_x + 2Q_y$, and two terms of the second-order of chromaticity which is independent to the angle e.g., $2Q_x$, $4Q_x$. The changes cause that the chaotic movement disappeared, and the area of DA improved as it is pictured in figure 10. The RDTs variation before and after optimization with OPA is shown in figure 11. Finally, we compare the DA of this lattice with the bare lattice in figure 12. From figure 12, the improvement after OPA optimization for off-momentum ($\frac{dp}{p} = 3\%$) in x and y plane and for on-momentum particles ($\frac{dp}{p} = 0$) in x plane is clear, although the DA for on-momentum particles in y plane does not show any improvement and it decreases. On the other hand, DA for particles which have a momentum deviation equal to $\frac{dp}{p} = -3\%$ remains constant. Overall, considering all types of the multiple errors (misalignment, FSE, and TILT) in all magnet elements, RF and synchrotron radiation in tracking, shows that the lattice which is optimized by MOGA has a better result in comparison with the lattice which is optimized by OPA, so we opt the MOGA optimized lattice as a final result for the ILSF storage ring. Also, we continue the GA optimization for the final lattice, too, but it does not show any big improvement after 16000 jobs.

6 Effect of errors and insertion device on the optimized lattice

The main limitation of dynamic aperture arises from the chromaticity of sextupoles. However, errors in magnetic elements and IDs can reduce the dynamic aperture too. In this section, we analyze the effect of multiple errors in magnetic elements and IDs on the area of DA and Touscheck lifetime that the rate of the errors are presented in table 4.

2020 JINST 15 P02009

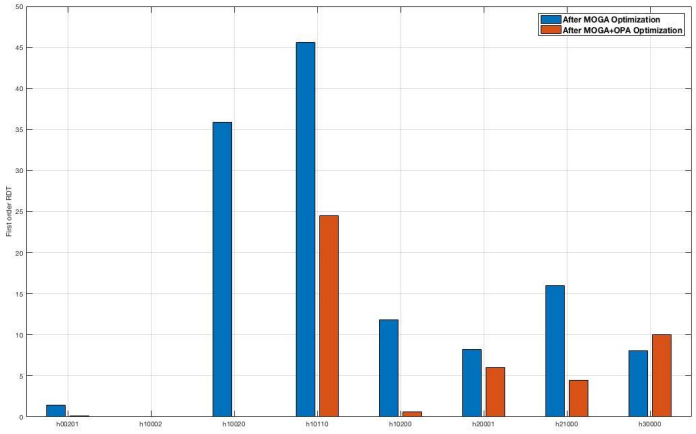

(a)

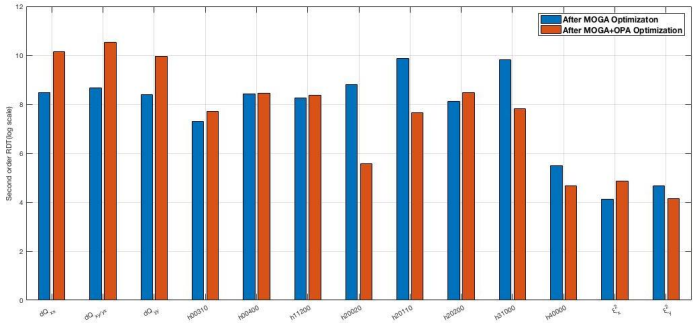

(b)

Figure 11. RDTs variation before and after optimization with OPA.

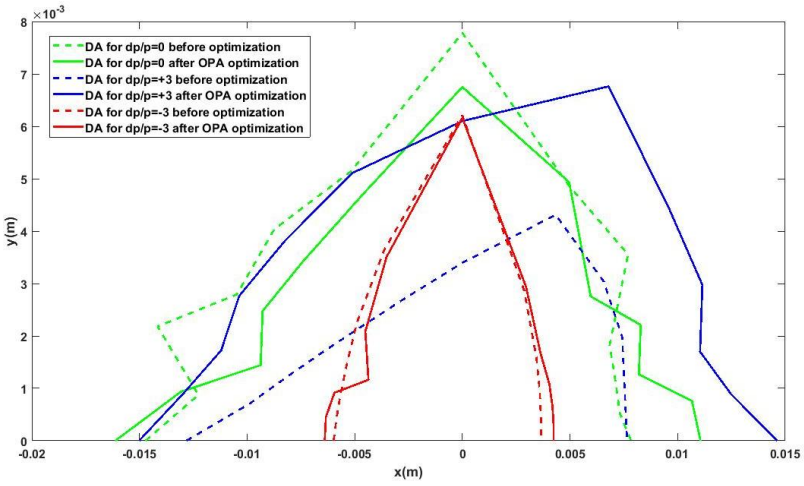

Figure 12. DA for optimized lattice with OPA (solid line) and bare lattice (dashed-line).

2020 JINST 15 P02009

Table 4. Type and rate of magnet errors in simulation.

Magnet	Type of Error	Rate of Error	Unit
Dipole	Misalignment in x direction	$40e-6$	m
	Misalignment in y direction	$40e-6$	m
	FSE	$1e-4$	-
	$ETILT$	$1e-4$	RAD
Quadrupoles	Misalignment in x direction	$40e-6$	m
	Misalignment in y direction	$40e-6$	m
	FSE	$40e-4$	-
	$TILT$	$1e-4$	RAD
Sextupoles	Misalignment in x direction	$40e-6$	m
	Misalignment in y direction	$40e-6$	m
	FSE	$40e-4$	-
	$TILT$	$1e-4$	RAD

Besides, the beta distortion in the presence of magnet errors leads to a larger beam size and may increase the effects of high order field and resonances [30], so before considering the effect of errors on DA, beta-beating should be corrected. We calculate the beta-beating as follow

$$\beta_{\text{beating}} = \frac{\beta - \beta_0}{\beta_0} \tag{6.1}$$

where β_0 is the beta function in the bare lattice, and β is the beta function for the lattice with the errors. Considering correctors in the middle of some sextupoles in the lattice, the beta-beating decreased to less than 10% in both directions, which is large for synchrotron light source. So, we applied LOCO [31] to correct the beta-distortion in this step. Regarding magnet errors which is considered in simulation, there is no closed orbit in the first tracking. So, the correction process starts with trajectory correction or pre-correction [32]. The results show that the maximum COD (Closed Orbit Distortion) for 100 random error distribution in horizontal and vertical planes before correction is 6 mm, and after correction, the rms COD calculates less than 70 and 60 μm for horizontal and vertical direction, respectively. The position of horizontal and vertical correctors, as well as BPMs, are pictured in figure 13a. One can see that 16 BPMs, 16 vertical and 16 horizontal correctors have been used for COD in each supercell. After correcting closed orbit, the linear parameters, e.g., dispersion and beta function, must be corrected. By changing the strength of quadrupoles, the beta-beating corrects to less than 1% and 1.5% in vertical and horizontal planes, respectively. The beta-distortion before and after correction is presented in figure 14. In addition, the dispersion before and after correction is shown in figure 15. The rate of quadrupoles changes and tune shift due to magnet errors before and after beta-beating correction are presented in tables 5 and 6. After beta-beating correction, DA tracks in Accelerator Toolbox for MATLAB [33], and the results are pictured in figure 16. One can see from figure 16 that because of the errors DA decreases, this reduction for $\frac{dp}{p} = 0$ particles is notable in both direction before beta-beating correction, while after beta-beating correction, DA improves. For off-momentum particles, result of the ideal lattice (without error) and the lattice which its beta-beating is corrected in the presence of all types of magnet errors, are presented in figure 16b. Also, the result of MA tracking is shown in figure 17.

2020 JINST 15 P02009

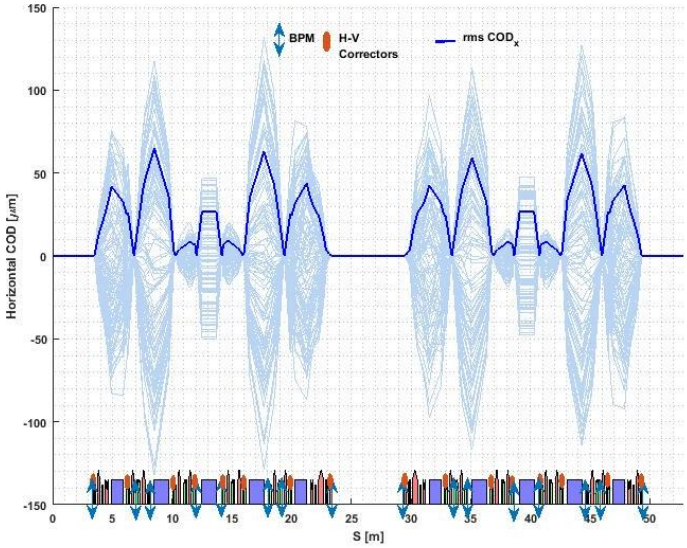

(a) Horizontal COD

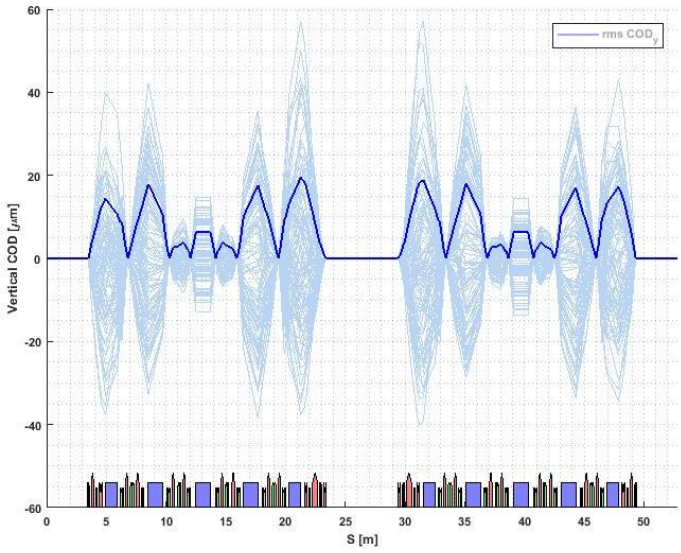

(b) Vertical COD

Figure 13. COD correction for 100 random error distribution.

The results in figure 17, show that after COD and beta-beating correction the MA improve in the lattice with magnet errors, but by considering the effect of RF and SR, we expect that the results show lower values. Also, the lifetime for the corrected lattice with magnet errors, without the effect of RF and SR is pictured in figure 18.

After sextupoles, IDs are the biggest nonlinearity at light sources and damping rings; there are two significant effects due to the perturbation of the electron beam by IDs in a ring that usually needs to consider, one of them is shift of the tune due to the magnetic field of the IDs, which results in beta-beating and a smaller dynamic aperture. The other is the change in emittance and energy spread of the electron beam due to the energy radiated from the IDs [34]. In continue, we consider

2020 JINST 15 P02009

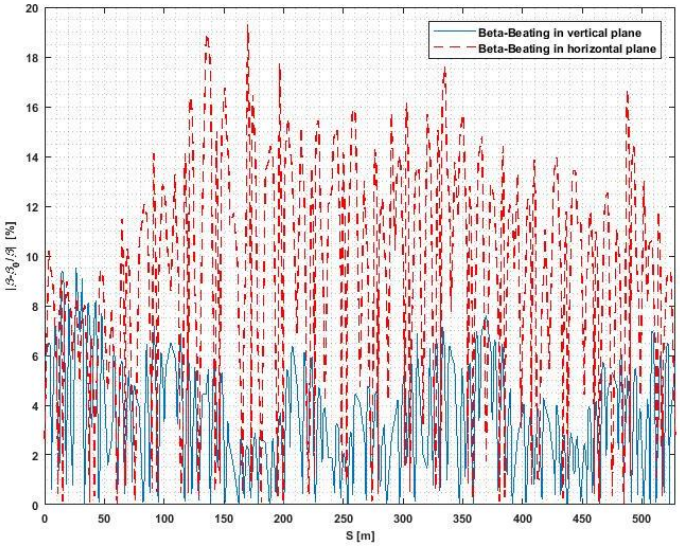

(a) Beta-beating before correction

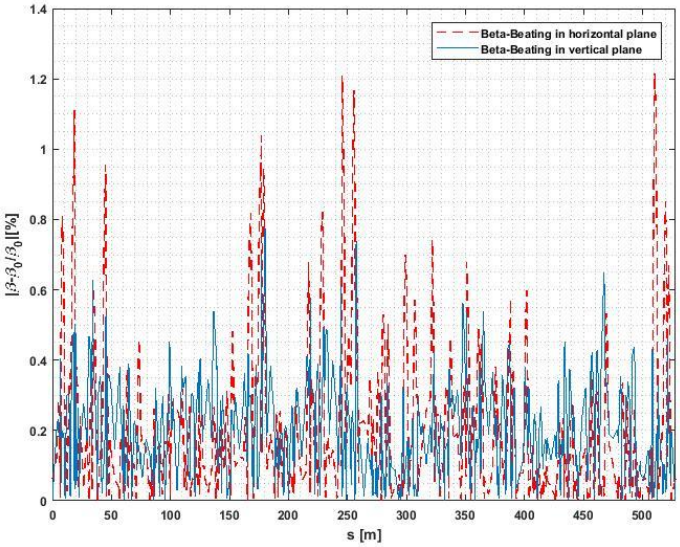

(b) Beta-beating after correction

Figure 14. Beta-distortion before and after correction.

the effect of Insertion Devices (IDs) on the beam. There are seven types of beamlines and IDs in the ILSF, which cover a wide spectral range (10 ev-30 kev). We calculate the influence of one of them, which is in-vacuum hybrid undulator (IVU) that extracts the micro-molecular (MX) beamline. The design and calculation of this ID that we called it U18 has finished, so we decided to put U18 in the low-beta lattice to see the effect of the ID on the dynamics of the electron beam, for more details about IDs and instabilities in the ILSF see refs. [35, 36]. We consider a $U18$ in the middle of the long straight section. In the presence of $U18$, the vertical beta function changes, while horizontal beta function does not change. The distorted beta function is compensated by three quadrupoles adjacent to ID, while the regular quadrupoles remain unchanged. The strengths of the quadrupoles nearest to

2020 JINST 15 P02009

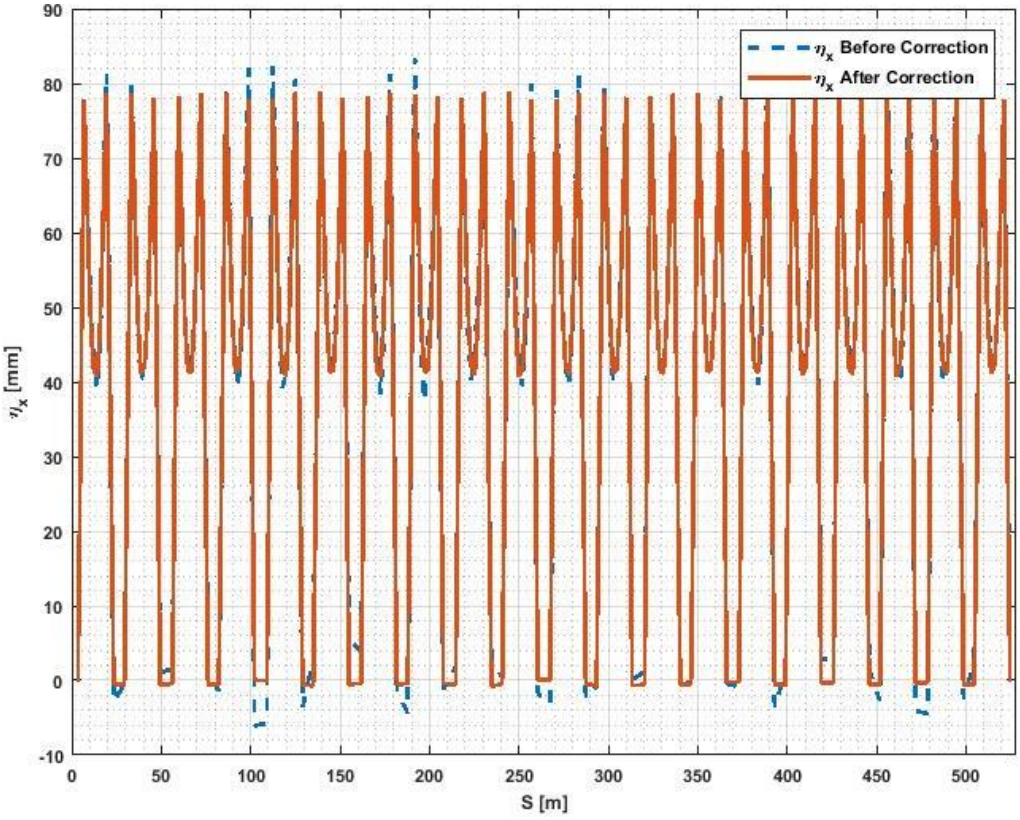

Figure 15. Dispersion before and after beta-beating correction.

Table 5. Gradient of quadrupoles in the low-beta lattice with magnets errors before and after beta-beating correction.

Quadrupole families	Original gradient ($\frac{T}{m}$)	Max Gradient with error after Beta-Beating correction ($\frac{T}{m}$)	Max Relative Change
Q1	4.0448	4.0960	0.120
Q2	3.2328	3.2773	0.130
Q3	2.8578	2.8761	0.010
Q4	3.5934	3.6161	0.010
QM1	3.8022	3.8093	0.002
QM2	−1.6616	−1.6500	0.007
QM3	−1.9816	−1.9716	0.005
QM4	2.8036	2.8073	0.001
QM5	−2.0918	−2.0837	0.004

$U18$ before and after beta correction present in table 7 and beta-beating before and after correction is displayed in figure 19. One can see that after correction, beta distortion decreases to less than 0.5%, except at the $U18$ location. DA and MA, in the presence of $U18$, show that DA decreases sharply in the vertical plane. The result of FMA and MA in the presence of one in-vacuum undulator is presented in figure 20 and 21. The Touschek lifetime for the lattice with ID will decrease too.

2020 JINST 15 P02009

Table 6. Effect of magnet errors and correction on tunes.

	Ideal Tune	Tune after COD correction	Tune after Beta-Beating correction
ν_x	46.2101	46.1945	46.2108
ν_y	17.3210	17.3407	17.3212

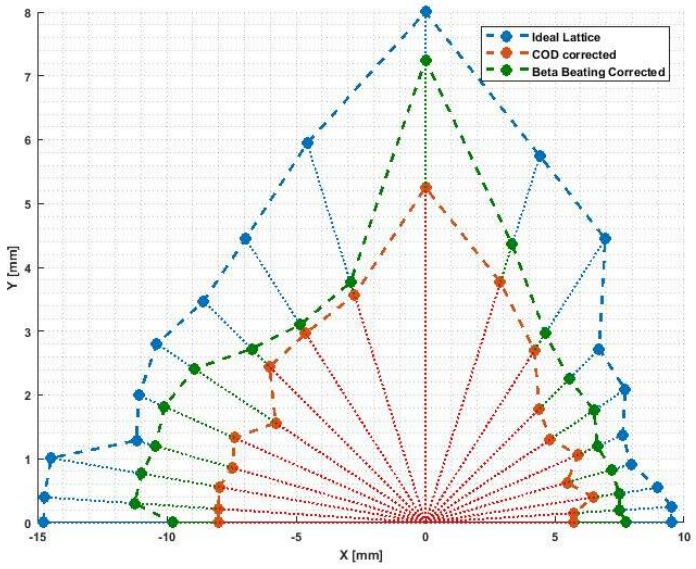

(a) On-momentum particles.

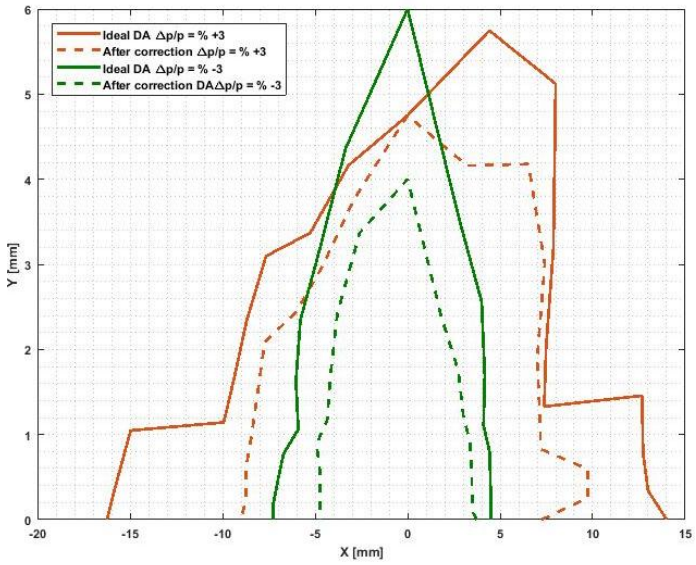

(b) Off-momentum particles.

Figure 16. DA by considering magnet errors for on- and off-momentum particles.

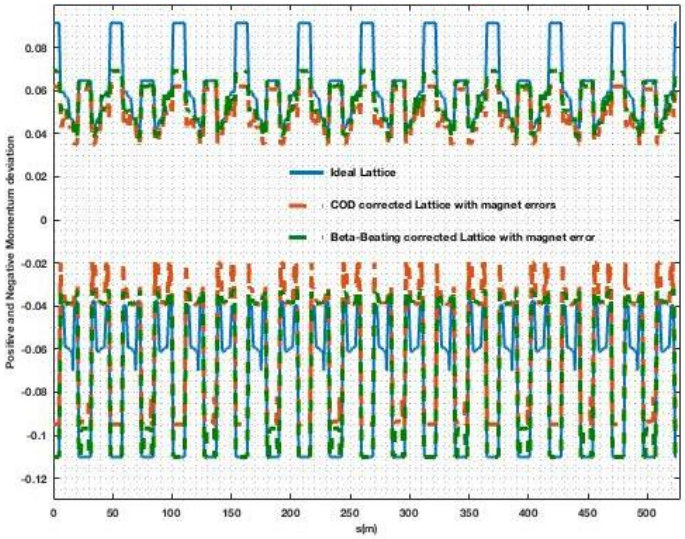

(a) MA in the ring

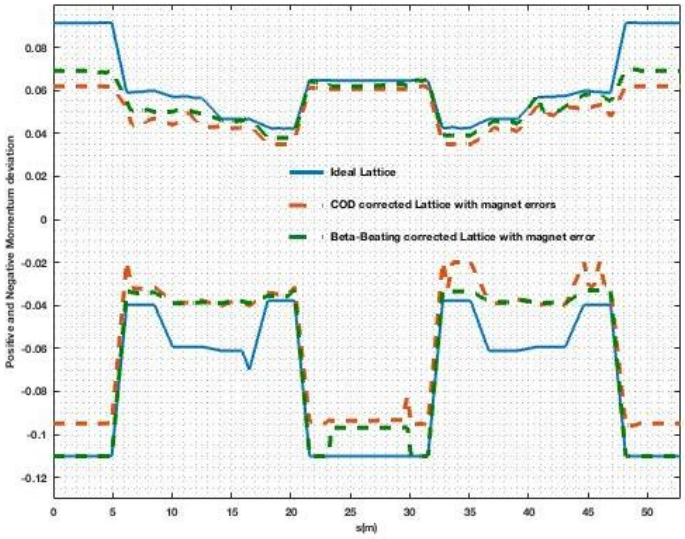

(b) MA in one super-period of the ring

Figure 17. MA for the corrected lattice with magnet errors without considering the effect of RF and SR.

Table 7. Gradient of adjacent quadrupoles to $U18$ before and after beta beating correction.

	Original gradient ($\frac{T}{m}$)	Gradient with $U18$ ($\frac{T}{m}$)	Relative Change
QD3U	−1.9816	−1.9820	2e-04
QF4U	2.8036	2.8055	6e-04
QD5U	−2.0918	−2.1040	5e-03

2020 JINST 15 P02009

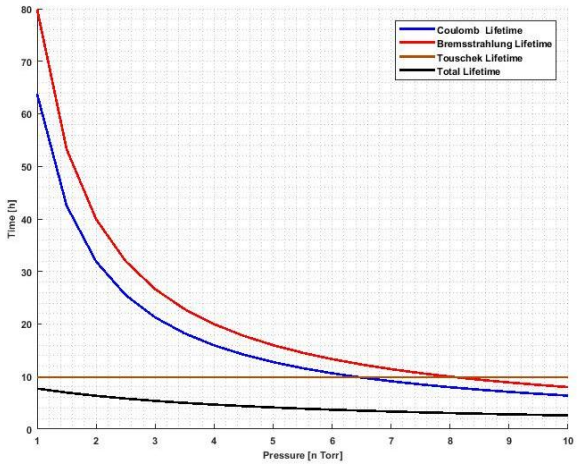

Figure 18. Lifetime for the bare corrected lattice with magnet error in different pressure.

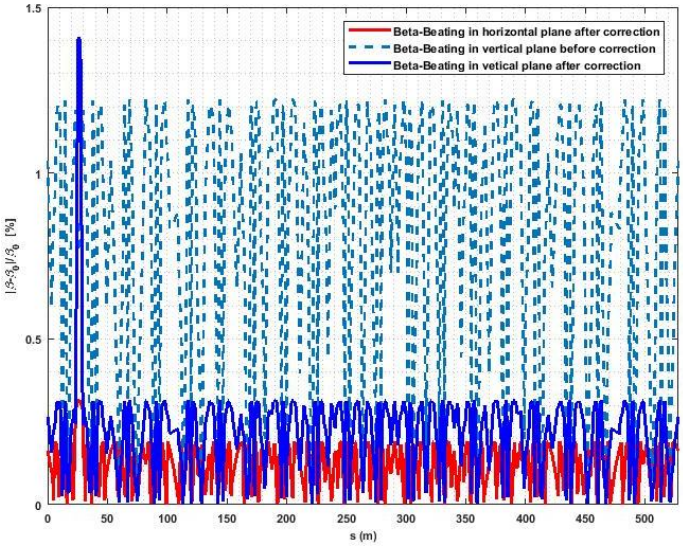

Figure 19. Beta-Beating along the ring with one in-vacuum undulator in a long straight section before and after correction. The peak points represent beta beating in $U18$.

7 Conclusion

The low-beta lattice for the ILSF storage ring is optimized by genetic algorithm. The linear and nonlinear optics are optimized simultaneously by MOGA to improve dynamic aperture and momentum acceptance without violation of constraints. It means that for each job, first, the four quadrupoles strength tuned, then the nonlinear optimization start. This method is straightforward, we need only to propose a possible lattice, and consider some twiss parameters as constraints. The code automatically searches for the low emittance lattice with better dynamic aperture and momentum acceptance. If there are feasible solutions, the algorithm will return the solutions with the best objectives, and the optimal global solution can be obtained. If not, it returns the solutions with the lowest constraint violation. The solutions are sorted based on Rank and CD by the NSGA-II sorting algorithm.

2020 JINST 15 P02009

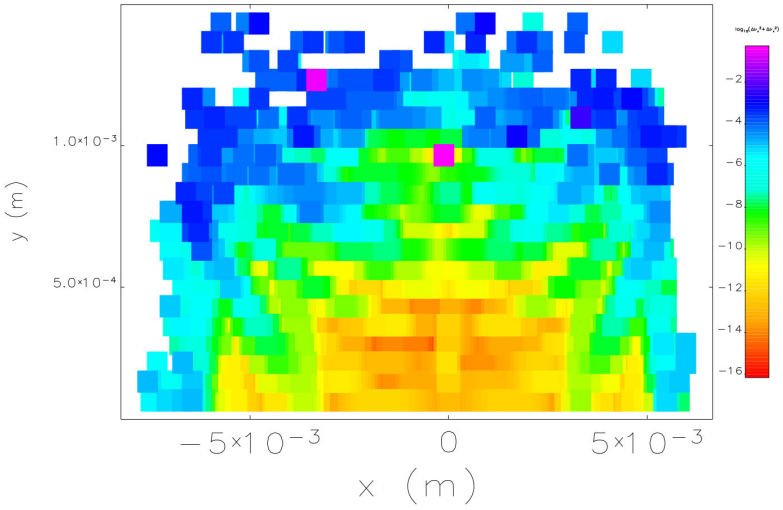

Figure 20. Frequency map with $U18$ at the center of a long straight section.

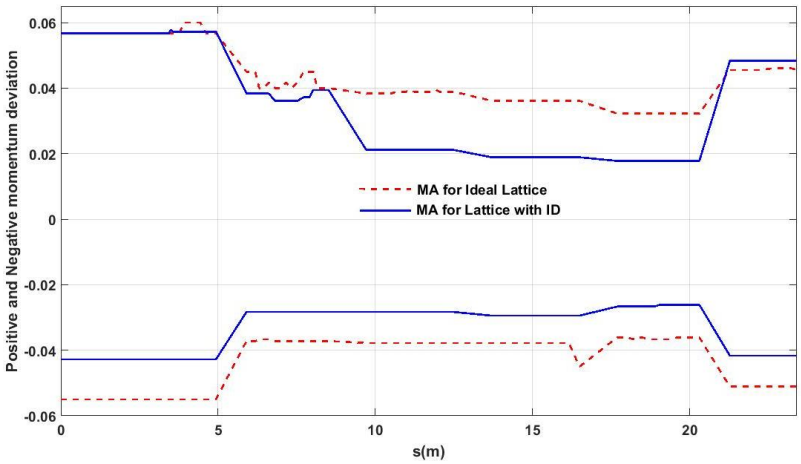

Figure 21. MA with $U18$ at the center of a long straight section.

Moreover, FMA and tune scan are applied to improve the results of MOGA optimization. The final analysis shows that by considering the effect of errors, RF, and SR, the lattice which is optimized by MOGA, shows a better performance. Finally, in the last section, the magnet errors and insertion device are considered in the optimized lattice to bring the final results closer to the realistic storage ring. The results show that in the presence of all magnet errors, after COD and beta-beating correction, DA and MA improve. In addition, in the presence of $U18$, DA in the horizontal plane does not change tremendously; however, it changes significantly in the vertical plane.

As a result, the performance of the low-beta lattice which has higher brilliance in comparison with the existing lattice is improved, while the emittance remains constant. However, the Touschek lifetime does not meet the needs, this defect can be covered by continuous injection, but the losses of beam may damaging fragments in the storage ring. Also, by increasing the length of the bunch, we can improve the Touschek lifetime too.

2020 JINST 15 P02009

Acknowledgments

This work was supported by Iranian Light Source Facility, Institute for Research in Fundamental Sciences.

References

[1] J. Rahighi et al., *Progress Status of the Iranian Light Source Facility Laboratory*, in *Proc. 5th Int. Particle Accelerator Conf. (IPAC 2014)*, Dresden, Germany, 16–20 June 2014, pp. 240–242 [DOI].

[2] E. Ahmadi, S.M. Jazayeri and J. Rahighi, *Characterizing and studying the nonlinear beam dynamics performance of Iranian Light Source Facility storage ring*, *Nucl. Instrum. Meth.* **A 927** (2019) 140.

[3] J. Rahighi et al., *Status Report on the Iranian Light Source Facility Project*, in *Proc. 3rd Int. Particle Accelerator Conf. (IPAC'12)*, New Orleans, LA, U.S.A., May 2012, paper TUEPPB008, pp. 1131–1133.

[4] OPA website, https://ados.web.psi.ch/opa/.

[5] T. Tanaka and H. Kitamura, *SPECTRA — a synchrotron radiation calculation code*, *J. Synchrotron Radiat.* **8** (2001) 1221.

[6] R. Hajima, N. Takeda, H. Ohashi and M. Akiyama, *Optimization of wiggler magnets ordering using a genetic algorithm*, *Nucl. Instrum. Meth.* **A 318** (1992) 1.

[7] I.V. Bazarov,*Overview of energy recovery linacs*, in *Proc. Particle Accelerator Conf.*, Knoxville, 2005, IEEE, Piscataway, NJ (2005), pp. 1382–386.

[8] F.E. Hannon and C. Hernandez-Garcia, *Simulation and Optimisation of a 100 mA DC Photo-Injector*, in *Proc. 10th Int. European Particle Accelerator Conf.*, Edinburgh, Scotland (2006), pp. 3550–3552.

[9] C.-X. Wang, *Simulation Study of a Normal-Conducting RF Photoinjector for ERL X-Ray Sources*, in *Proc. 23rd Int. Particle Accelerator Conf.*, Vancouver, Canada, 2009, IEEE, Piscataway, NJ (2009), pp. 467–469.

[10] X. Dong, C.X. Wang, A. Zholents, K.J. Kim and N. Sereno, *Development of an Ultra-Low-Emittance RF PhotoInjector for a Future X-Ray FEL Oscillator*, in *Proc. Particle Accelerator Conf.*, NY, U.S.A., 2011, IEEE, New York (2011), pp. 2005–2007.

[11] I.V. Bazarov and C.K. Sinclair, *Multivariate optimization of a high brightness dc gun photoinjector*, *Phys. Rev. ST Accel. Beams* **8** (2005) 034202.

[12] I.V. Bazarov, I. Senderovich and C.K. Sinclair, *Use of multiobjective evolutionary algorithms in high brightness electron source design*, in *Proc. Particle Accelerator Conf.*, Knoxville, 2005, IEEE, Piscataway, NJ (2005), pp. 2188–2190.

[13] M. Borland, V. Sajaev, L.E. Emery, A. Xiao and Accelerator Systems Division, *Multi-objective direct optimization of dynamic acceptance and lifetime for potential upgrades of the Advanced Photon Source*, Technical Report (2010). [DOI].

[14] J. Bengtsson, *The Sextupoles Scheme for the Swiss Light Source (SLS): An Analytic Approach*, SLS Note 9/97 (1997) [https://ados.web.psi.ch/slsnotes/sls0997.pdf].

[15] S. Fartoukh, *Second order chromaticity correction of LHC V6.0 at collision*, CERN-LHC-PROJECT-REPORT-308.

[16] G. Kumar, *The Multi-Objective Genetic Algorithm Based Techniques for Intrusion Detection*, *Int. J. Adv. Res. Comput. Sci. Software Eng.* **1** (2014) 14.

[17] A. Hofler et al., *Innovative applications of genetic algorithms to problems in accelerator physics*, *Phys. Rev. ST Accel. Beams* **16** (2013) 010101.

2020 JINST 15 P02009

[18] D.W. Corne, N.R. Jerram, J.D. Knowles, M.J. Oates and J. Martin, *PESA-II: Region-based Selection in Evolutionary Multiobjective Optimization*, in *Proc. GECCO'2001* (2001), pp. 283–290.

[19] E. Zitzler, K. Deb and L.Thiele, *Comparison of multiobjective evolutionary algorithms: Empirical results*, *Evol. Comput.* **8** (2000) 173.

[20] K. Deb, S. Agrawal, A. Pratap and T. Meyarivan, *A Fast Elitist Non-dominated Sorting Genetic Algorithm for Multi-objective Optimization: NSGA-II*, in *Parallel Problem Solving from Nature PPSN VI*, PPSN 2000, Lecture Notes in Computer Science, vol. 1917, M. Schoenauer et al. eds., Springer, Berlin, Heidelberg (2000).

[21] N. Srinivas and K. Deb, *Muiltiobjective Optimization Using Nondominated Sorting in Genetic Algorithms*, *Evol. Comput.* **3** (1994) 221.

[22] J. Hasanpour, M. Ghodoosi and Z. Hosseini, *Optimizing a bi-objective preemptive multi-mode resource constrained project scheduling problem: NSGA-II and MOICA algorithms*, DOI (2016).

[23] C. Sun, D.S. Robin, H. Nishimura, C. Steier and W. Wan, *Small-emittance and low-beta lattice designs and optimizations*, *Phys. Rev. ST Accel. Beams* **15** (2012) 054001.

[24] R. Tomas, M. Giovannozzi and R. de Maria, *Nonlinear correction schemes for the phase 1 LHC insertion region upgrade and dynamic aperture studies*, *Phys. Rev. ST Accel. Beams* **12** (2009) 011002.

[25] W. Gao, L. Wang and W. Li, *Simultaneous optimization of beam emittance and dynamic aperture for electron storage ring using genetic algorithm*, *Phys. Rev. ST Accel. Beams* **14** (2011) 094001.

[26] W. Wan and J.R. Cary, *Method for enlarging the dynamic aperture of accelerator lattices*, *Phys. Rev. ST Accel. Beams* **4** (2001) 084001.

[27] C. Steier, D. Robin, W. Decking, J. Laskar, L. Nadolski and Y. Wu, *Measuring and Understanding the Momentum Aperture in a Storage Ring*, in *Proc. IPAC'2005*, Knoxville, TN, U.S.A., 16–20 May 2005, pp. 645–649.

[28] M. Borland, *elegant: A Flexible SDDS-Compliant Code for Accelerator Simulation*, Advanced Photon Source LS-287, September 2000.

[29] M. Borland, *A self-describing file protocol for simulation, integration, and shared post-processors*, in *Proc. 1995 Particle Accelerator Conf.*, Dalla, Texas (1995), pp. 2184.

[30] Y. Nosochkov and J. Corbett, *Dynamic aperture studies for SPEAR 3*, *AIP Conf. Proc.* **468** (1999) 25 [physics/0106066].

[31] G. Portmann, J. Safranek and X. Huang, *Matlab based LOCO*, *ICFA Beam Dyn. Newslett.* **44** (2007) 49.

[32] A. Mashal, F.D. Kashani and J. Rahighi, *Linear optics and coupling correction of ILSF storage ring lattice*, *Nucl. Instrum. Meth.* **A 953** (2020) 163180.

[33] A. Terebilo, *Accelerator toolbox for MATLAB*, SLAC-PUB-8732.

[34] L. Smith,*Effects Of Wigglers And Undulators On Beam Dynamics*, in *Novosibirsk 1986, Proceedings, High energy accelerators*, vol. 2, pp. 130–133 and Lawrence Berkeley Lab., LBL-21391 (86, rec. Nov.) pp. 3.

[35] M. Hadad, S. Dastan, J. Rahighi, M. Razazian, F. Saeidi and S. Yousefnejad, *Insertion Devices for the Day-One Beamlines of ILSF*, in *Proc. IPAC'19*, Melbourne, Australia, May 2019, pp. 1561–1563.

[36] N. Khosravi et al., *A General Comparison On Impedance Theory And Cst Simulation of Discontinuities*, *J. Phys. Conf. Ser.* **1350** (2019) 012122.

2020 JINST 15 P02009